Improved Demagnetization Control of a Doubly-Fed Induction Generator Under Balanced Grid Fault

Linyuan Zhou, *Student Member, IEEE*, Jinjun Liu, *Senior Member, IEEE*, and Sizhan Zhou, *Student Member, IEEE*

***Abstract*—Doubly-fed induction generators are one of the most popular machines for variable-speed wind turbine. However, they are very sensitive to grid fault since the stator is directly connected to the grid. This paper analyzes the low-voltage ride-through performance of a doubly-fed induction generator-based wind turbine under balanced grid fault. An improved demagnetization control, immune to system parameter variation, is proposed to shorten the dynamic process. The investigation shows that the proposed method increases the probability of a successful ride-through at the recovery moment of balanced grid fault. Feasibility region for a representatively sized system is also investigated for balanced grid fault. In order to verify the proposed control method, laboratory experiments are carried out and the results demonstrate the analysis.**

***Index Terms*—Demagnetization control, doubly-fed induction generator (DFIG), low-voltage ride-through (LVRT).**

NOMENCLATURE

De, NDe	Subscript denoting system with and without demagnetization control.
r	Superscript denoting rotor reference frame.
f, n	Subscript denoting variable corresponding to forced and natural component.
$\vec{i}_d$, $\vec{i}_q$	Reactive and active current.
$\vec{i}_m$, $\vec{i}_r$, $\vec{i}_s$	Magnetizing rotor and stator current.
$I_{r\_\max}$	Maximum allowed rotor current.
L_m, L_{lr}, L_{ls}	Magnetizing rotor and stator leakage inductance.
L_r, L_s	Rotor and stator inductance.
R_r, R_s	Rotor and stator resistance.
$\vec{v}_r$, $\vec{v}_s$	Rotor and stator terminal voltage.
ω, ω_s	Rotor and synchronous angular frequency.
$\vec{\psi}_r$, $\vec{\psi}_s$	Rotor and stator flux.

I. INTRODUCTION

WIND energy is now playing an important role in the grid. Doubly-fed induction generators (DFIG) are one of the most employed generators due to the advantages of variable-speed-based operation and decoupled control of active and reactive power. Moreover, the converter is rated at around 30% of the generator rating, which takes advantage of small size, light weight, low cost, and small losses compared to full-scale power converters [1].

Originally, the generator unit was disconnected from the grid to protect the converter on detecting a grid fault. This is allowed when the wind power represents only an insignificant part of the generation in the system. As the penetration of the wind power system gets higher and higher, wind farms are now required to remain connected to the grid for a given time duration during grid fault and actively contribute to the power system stability by supplying reactive power, known as the low-voltage ride-through (LVRT) requirement [2]. However, since the stator of the DFIG is directly connected to the grid, the machine is very sensitive to grid disturbance, especially to grid dips. Natural stator flux is produced at the grid fault moment [3] and negative sequence stator flux is generated under unbalanced grid fault [4]. The natural and negative sequence stator flux induces very high electromotive force (EMF) in the rotor circuit. If the rotor-side converter (RSC) cannot compensate for the induced EMF, a large transient rotor current appears, leading to the destruction of the converter and disconnection of the system.

The state-of-the-art LVRT solution is the employment of a crowbar [5]. On detecting of the rotor overcurrent, the crowbar short circuits the rotor terminal and the trigging signal of the RSC is blocked at the same time, providing conservative protection to the system. However, it changes the DFIG into a regular induction machine, which absorbs reactive power, further deteriorating the grid fault. As a result, dynamic VAR compensators are sometimes installed at the DFIG terminals to provide reactive power during grid faults [6].

Researchers are now addressing the issue from other points of view. Alternative solutions based on extra power electronic equipment are proposed. For instance, some authors have proposed schemes with an additional grid-side converter (GSC) [7], [8], dynamic voltage restorer [9], [10], and energy storage system [11], but the high cost and control complexity discourages their utilization. The implementation of a stator-side passive impedance network [12], rotor-side dynamic resistor [13], and rotor-side reactor [14] are also proposed. In this way, the wind turbine can remain connected to the grid during grid dips. However, sizing of the impedance is made either experimentally or by simulation, and therefore, it is quite difficult to optimize the whole system.

Solutions based on advanced control methods are attractive due to the advantage of easy implementation. It has been demonstrated that feed-forward transient current control (FFTCC) could limit transient rotor current during grid faults, resulting in minimum occurrence of crowbar interruptions [15], [16]. Stator current was feedback as the rotor current reference in [17]. However, the torque is fixed to zero and the reactive power must

Manuscript received March 14, 2014; revised August 14, 2014; accepted December 5, 2014. Date of publication December 18, 2014; date of current version August 21, 2015. This work was supported by the Major Program of the National Natural Science Foundation of China under Grant 51437007. Recommended for publication by Associate Editor J. A. Pomilio.

The authors are with the State Key Lab of Electrical Insulation and Power Equipment, School of Electrical Engineering, Xi'an Jiaotong University, Xi'an 710049, China (e-mail: zhoulyamil@163.com; jjliu@mail.xjtu.edu.cn; zhousizhan@gmail.com).

Color versions of one or more of the figures in this paper are available online at http://ieeexplore.ieee.org.

Digital Object Identifier 10.1109/TPEL.2014.2382603

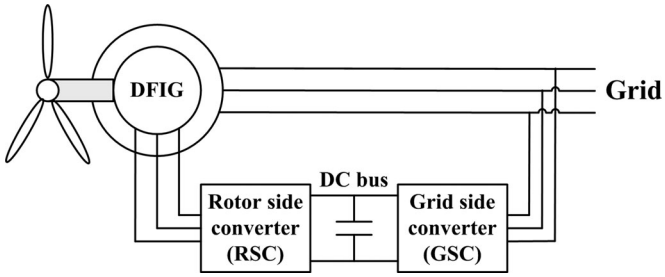

Fig. 1. Wind turbine scheme with DFIG.

be drawn from the grid. A similar but more general idea of stator flux tracking-based LVRT control strategy is proposed [18], which provides an additional freedom named tracking gain to improve the performance, but the same problem as that in [17] cannot be avoided.

Demagnetization control was proposed to counteract the natural and negative sequence components of the stator flux [19], and it has been proven that the control could promote natural stator flux damping [20]. Combination of demagnetization control and active crowbar is proposed to shorten the crowbar activation time [21]. However, the demagnetization control in the aforementioned research works is sensitive to system parameter variation since stator resistance information is needed, in spite of that the sensitivity can be reduced when demagnetization control is combined with virtual resistance [22].

This paper extends the initial study presented in [23] and [24] and proposes an improved demagnetization control approach for the DFIG, immune to system parameter variation. With the demagnetizing rotor current, transient response of the system can be notably accelerated and system LVRT capability is improved under balanced fault.

This paper is organized as follows. Section II analyzes system behavior during and after balanced grid fault. It shows that the natural EMF after the fault clearance is influenced by fault duration and stator flux time constant. Section III introduces the proposed demagnetization control, and the influence on the LVRT performance is discussed in Section IV. It is proved that system LVRT capability can be improved by reducing the EMF and minimizing the occurrence of the protection system at the recovery moment of balanced grid fault. Feasibility region of a typical MW-level DFIG system is also investigated. Finally, the proposed control method and the analysis are verified on a laboratory test bed in Section V.

II. System Operation Under Balanced Grid Fault

The basic configuration of a DFIG-based wind turbine is shown in Fig. 1. The RSC regulates the rotational speed of the wind turbine to capture desired wind power, while the dc bus voltage is controlled by the GSC. System behavior under the shallow grid fault, where the rotor current remains under control, is analyzed in this section. For severe grid fault, overcurrent is generated, trigging the protection system. With the activation of crowbar, the DFIG changes to a regular induction generator, where a detailed analysis is given in [25].

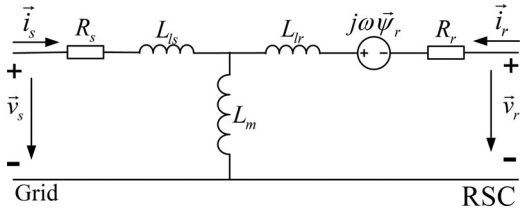

Fig. 2. Park model of DFIG in stationary reference frame.

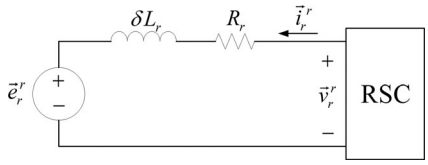

Fig. 3. Equivalent circuit of DFIG in rotor reference frame.

A. Park Model

The Park model of the DFIG in stationary reference frame [3] is used here, as illustrated in Fig. 2. For simplicity, the rotor variables are referred to the stator in this paper. Using motor convention, the equations are expressed as

$$\vec{\psi}_s = L_s\vec{i}_s + L_m\vec{i}_r \tag{1}$$

$$\vec{\psi}_r = L_r\vec{i}_r + L_m\vec{i} \tag{2}$$

$$\vec{v}_s = R_s\vec{i}_s + d\vec{\psi}_s/dt \tag{3}$$

$$\vec{v}_r = R_r\vec{i}_r + d\vec{\psi}_r/dt - j\omega\vec{\psi}_r. \tag{4}$$

The rotor voltage can then be got and divided into two terms, given as [3]

$$\vec{v}_r = \frac{L_m}{L_s}\left(\frac{d}{dt} - j\omega\right)\vec{\psi}_s + \left[R_r + \sigma L_r\left(\frac{d}{dt} - j\omega\right)\right]\vec{i}_r \tag{5}$$

where $\sigma = 1 - L_m^2/L_sL_r$ is the leakage coefficient. The first term, denoted $\vec{e}_r$, is the EMF induced by the stator flux. The second term is the voltage drop in the rotor circuit impedance. The rotor voltage and the EMF, expressed in the rotor reference frame, are given as [21]

$$\vec{v}_r^r = \frac{L_m}{L_s}\frac{d\vec{\psi}_s^r}{dt} + \left(R_r + \sigma L_r\frac{d}{dt}\right)\vec{i}_r^r \tag{6}$$

$$\vec{e}_r^r = \frac{L_m}{L_s}\frac{d}{dt}\vec{\psi}_s^r. \tag{7}$$

The equivalent circuit of DFIG, seen from the RSC, can be obtained according to (6) and is shown in Fig. 3. With a small rotor circuit impedance, $\vec{v}_r^r$ does not differ substantially from $\vec{e}_{rf}^r$. Considering the safety margin for dynamic process and constrained slip, which typically locate within -0.3 to 0.3, the rated voltage of RSC is limited to about 40% of the rated stator voltage [3].

B. System Behavior Under Balanced Grid Fault

The DFIG is assumed to be working under normal condition when a balanced voltage dip of depth P occurs at time t_0 and recovers at time t_1. The expression of the grid voltage is given as

$$\vec{v}_s = \begin{cases} V_s e^{j\omega_s t}, & (t < t_0) \\ (1-P)\, V_s e^{j\omega_s t}, & (t_0 \le t < t_1) \\ V_s e^{j\omega_s t}, & (t_1 \le t)\,. \end{cases} \tag{8}$$

1) System Responses in Normal Condition: Neglecting stator resistance for the small value, the steady-state stator flux can be obtained according to (3) and (8)

$$\vec{\psi}_s = V_s e^{j\omega_s t}/(j\omega_s) = \Psi_s e^{j\omega_s t - \pi/2} \qquad (t < t_0)\,. \tag{9}$$

Since stator flux given by (9) is dictated by grid voltage and represents the forced response of the system, it is referred to as forced stator flux $\vec{\psi}_{sf}$. As can be seen, $\vec{\psi}_{sf}$ rotates synchronously and its amplitude is proportional to the grid voltage. By substituting (9) into (7), the forced EMF is shown as

$$\vec{e}_{rf} = \frac{L_m}{L_s} s V_s e^{js\omega_s t - \pi/2} \tag{10}$$

where s is slip.

Neglecting the leakage inductance, the forced magnetizing current can be obtained according to (1) and (9), given approximately as

$$\vec{i}_{mf} \approx \Psi_{sf} e^{j\omega_s t - \pi/2}/L_m = I_{mf} e^{j\omega_s t - \pi/2}. \tag{11}$$

Whenever current flows through an inductor, a magnetic field is generated and energy is stored at the same time. For the DFIG, the energy stored in the magnetic field, denoted E_{mf}, is a dc value in the steady state and proportional to the square of grid voltage.

2) Stator Flux Responses Under Balanced Grid Fault: Unlike grid voltage, the stator flux cannot change instantaneously at time t_0, which would make the magnetic state of the machine change instantaneously and cannot happen in a practical point of view [3]. In contrast, the stator flux changes progressively. Natural stator flux is generated to guarantee the continuity of stator flux and magnetic energy. The DFIG can then be represented by a natural machine with the natural stator component and a forced machine corresponding to the line frequency stator component, as shown in Fig. 4.

By means of (1) and (3), the stator flux is related to stator voltage and rotor current by

$$\frac{d\vec{\psi}_s}{dt} = \vec{v}_s - \frac{R_s}{L_s}\vec{\psi}_s + \frac{L_m}{L_s} R_s \vec{i}_r. \tag{12}$$

With FFTCC, natural EMF can be accurately estimated and thus be fully compensated for under shallow grid fault [15], making the RSC behave like an open circuit to the natural stator component, which will be proven experimentally later. The natural stator flux is then merely induced by the natural stator current, which circulates in the mesh shown in Fig. 4(a) and can be obtained according to (1)

$$\vec{i}_{sn}(t_{0+}) = \vec{\psi}_{sn}(t_{0+})/L_s. \tag{13}$$

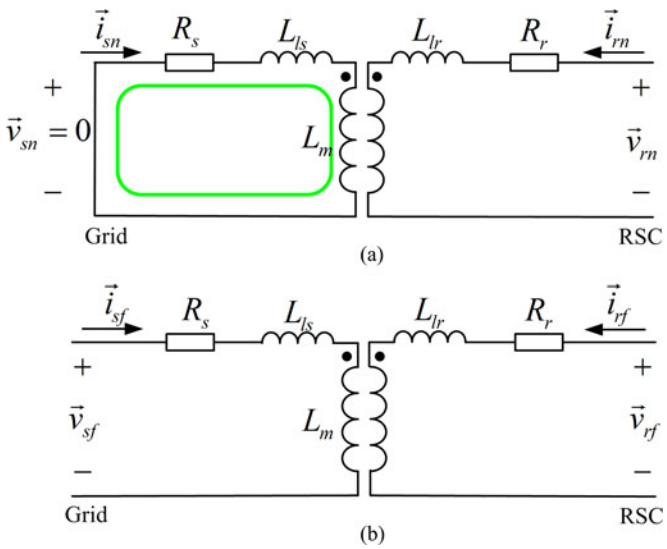

Fig. 4. Equivalent model of DFIG. (a) Natural machine. (b) Forced machine.

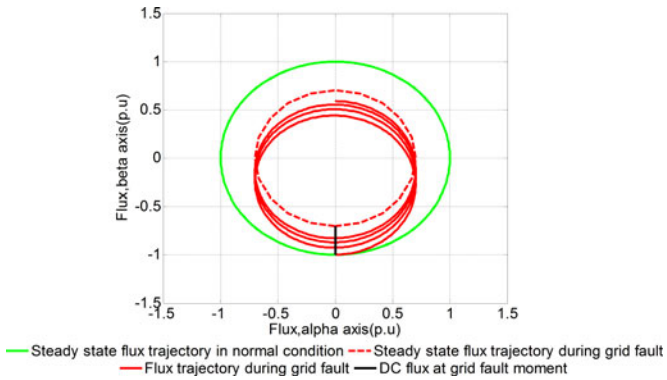

Fig. 5. Stator flux trajectory for a 30% balanced grid fault.

The reduction of the forced magnetic energy corresponding to the grid fault, which is consumed by the stator resistance with the flowing of natural stator current, is given as

$$\Delta E_{mf} = \left(2P - P^2\right) E_{mf}. \tag{14}$$

Considering $\vec{i}_{rn} = 0$, evolution of the forced and natural stator flux during grid fault can be derived from (8), (9), and (12)

$$\vec{\psi}_{sf} = (1-P)\, V_s e^{j\omega_s t}/(j\omega_s) \quad (t_0 \le t < t_1) \tag{15}$$

$$\vec{\psi}_{sn} = \vec{\psi}_{sn}(t_{0+})\, e^{-(t-t_0)/\tau_s} = P V_s e^{j\omega_s t_0} e^{-(t-t_0)/\tau_s}/(j\omega_s) \quad (t_0 \le t < t_1) \tag{16}$$

where $\tau_s = L_s/R_s$ is the stator flux time constant.

It is noticed that the natural stator flux is a dc component and has constant direction with respect to the stator winding. Therefore, it is also named dc stator flux [3]. Fig. 5 shows the stator flux trajectory for a 30% p.u. balanced grid fault. During the transient process, the dc stator flux damps exponentially according to the stator flux time constant.

Similarly, natural stator flux is generated at the grid fault recovery time t_1. With (8), (12), (15), (16), and $\vec{i}_{rn} = 0$, the

stator flux after t_1 is expressed as

$$\vec{\psi}_{sf} = V_s e^{j\omega_s t}/(j\omega_s) \quad (t_1 \le t) \tag{17}$$

$$\vec{\psi}_{sn} = \vec{\psi}_{sn}(t_{1+}) e^{-(t-t_1)/\tau_s} = \left(e^{-\Delta t/\tau_s} - e^{j\omega_s \Delta t}\right) \times e^{j\omega_s t_0} e^{-(t-t_1)/\tau_s} PV/(j\omega_s) \quad (t_1 \le t) \tag{18}$$

where $\Delta t = t_1 - t_0$ is the fault duration.

Comparing (16) with (18), it is noticed that $\left|\vec{\psi}_{sn}(t_{0+})\right|$ is solely dictated by grid fault depth *P*, while $\left|\vec{\psi}_{sn}(t_{1+})\right|$ is determined by grid fault depth *P* together with fault duration Δt and stator flux time constant τ_s. Taking $\left|\vec{\psi}_{sn}(t_{0+})\right|$ as the base value, the normalized value of $\left|\vec{\psi}_{sn}(t_{1+})\right|$ is given as

$$\left|\vec{\psi}_{sn\_\text{p.u.}}(t_{1+})\right| = \left|e^{-\Delta t/\tau_s} - e^{j\omega_s \Delta t}\right|. \tag{19}$$

3) Rotor Circuit EMF Response Under Balanced Grid Fault: During the transient process of grid fault and recovery, the EMF is composed of two components, induced by the forced and natural stator flux, respectively. Substituting (15)–(18) into (7), we can obtain the forced and natural EMF given as

$$\vec{e}^{r}_{rf} = \begin{cases} s\frac{L_m}{L_s} \cdot (1-P) V_s e^{js\omega_s t} & (t_0 \le t < t_1) \\ s\frac{L_m}{L_s} \cdot V_s e^{js\omega_s t} & (t_1 \le t) \end{cases} \tag{20}$$

$$\vec{e}^{r}_{rn} = \begin{cases} -(1/\tau_s + j\omega)\frac{L_m}{L_s} e^{-(t-t_0)/\tau_s} e^{-j\omega t} \vec{\psi}_{sn}(t_{0+}) & (t_0 \le t < t_1) \\ -(1/\tau_s + j\omega)\frac{L_m}{L_s} e^{-(t-t_1)/\tau_s} e^{-j\omega t} \vec{\psi}_{sn}(t_{1+}) & (t_1 \le t). \end{cases} \tag{21}$$

Neglecting $1/\tau_s$ for the small value, the natural EMF can be simplified as

$$\vec{e}^{r}_{rn} \approx \begin{cases} -(1-s)\frac{L_m}{L_s} PV_s e^{j\omega_s t_0} e^{-(t-t_0)/\tau_s} e^{-j(1-s)\omega_s t} & (t_0 \le t < t_1) \\ -(1-s)\frac{L_m}{L_s} PV_s \left(e^{j\omega_s t_0} e^{-\Delta t/\tau_s} - e^{j\omega_s t_1}\right) \times e^{-(t-t_1)/\tau_s} e^{-j(1-s)\omega_s t} & (t_1 \le t). \end{cases} \tag{22}$$

The forced EMF is small since it is proportional to the slip s. In contrast, the natural EMF is proportional to the term "$1-s$," which may reach a very high value.

III. Demagnetization Control

The DFIG is usually controlled by means of a vector control, where detailed description can be found in [26]. This paper will focus on the control of RSC and the GSC will not be considered.

To mitigate the influence of natural stator flux and improve system LVRT capability under balanced grid fault, an improved demagnetization control, which does not need system parameter information, is proposed here. The layout of the control approach is shown in Fig. 6. Demagnetizing rotor current, which opposes the natural stator current, is injected into the rotor

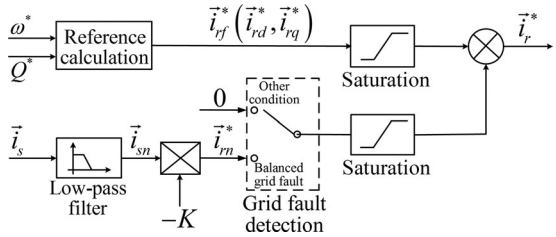

Fig. 6. Control block diagram of the improved demagnetization control.

circuit on detecting of a balanced grid fault. The reference is given as

$$\vec{i}^{*}_{rn} = -K\vec{i}_{sn} \tag{23}$$

where *K* is a positive demagnetization coefficient.

The relationship of $\vec{\psi}_{sn}$ and $\vec{i}_{sn}$ can then be obtained from (1) and (23)

$$\vec{i}_{sn} = \vec{\psi}_{sn}/(L_s - KL_m). \tag{24}$$

With (3), (24), and $\vec{v}_{sn} = 0$, the expression of natural stator flux is given as

$$\vec{\psi}_{sn} = \vec{\psi}_{\text{n0}}(t_0) e^{-t/\tau_s'} \quad (t \ge t_0) \tag{25}$$

where $\tau_s' = (L_s - KL_m)/R_s$ is the stator flux time constant with demagnetization control.

Comparing (16) with (25), it is obvious that the damping of natural stator flux is accelerated with positive *K*. To shorten the dynamic process, it is desirable to have a small time constant τ_s', which indicates a large demagnetization coefficient *K*. However, τ_s' turns negative if *K* is too large, making the natural stator flux increase instead of decay. Setting τ_s' to zero, the critical demagnetization coefficient can be obtained as

$$K_{\text{critical}} = L_s/L_m. \tag{26}$$

In practice, *K* can be set to a fixed value, or dynamically modified according to system working condition. To guarantee the stability of the system, it is strongly recommended that the maximum K should be limited to 1, which is a little bit smaller than the critical value.

The active and reactive current can be supplied together with the demagnetizing current during grid fault. The total rotor current then results from the addition of $\vec{I}^{*}_{rd}$, $\vec{I}^{*}_{rq}$, and $\vec{I}^{*}_{rn}$. Since the overall current should be constrained to the maximum allowed rotor current $I_{r\_\max}$, coordination has to be made. In this paper, reactive power is preferentially guaranteed. The reactive current required by STATE GRID Corporation of China is $I_d^* = 1.5 \cdot (0.9\,V_s - V_{s\_\text{fault}})$, making the amplitude of reactive current reference $I_{rd}^* = \min(I_{d,}^* I_{r\_\max})$. To promote dc stator flux damping, we prioritize demagnetizing current over the active current. The maximum allowed demagnetizing current can then be obtained as $I_{rn\_\max} = I_{r\_\max} - I_{rd}^*$. Finally, the active current is constrained to the remaining rotor current rating.

With the injection of demagnetizing rotor current, the natural stator current at time t_{0+} can be derived according to (24)

$$\vec{i}_{sn}(t_{0+}) = \vec{\psi}_{sn}(t_{0+})/(L_s - KL_m). \tag{27}$$

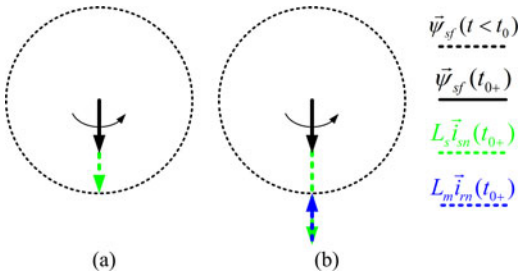

Fig. 7. Stator flux trajectory at grid fault moment. (a) Without demagnetization control. (b) With demagnetization control.

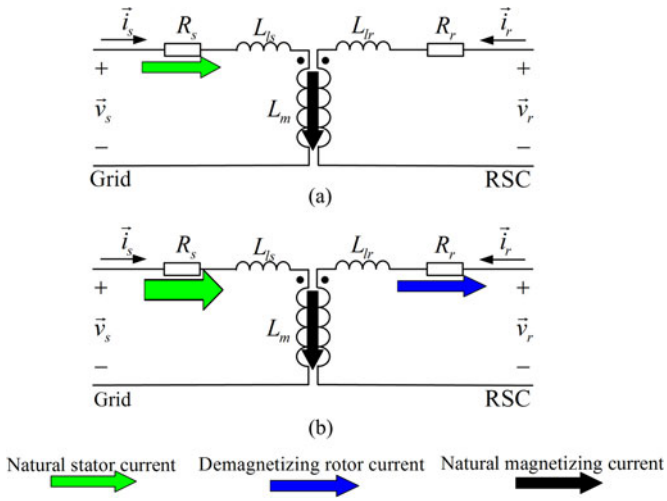

Fig. 8. Natural current of the system. (a) Without demagnetization control. (b) With demagnetization control.

Comparing (13) with (27), it is obvious that we have higher natural stator current with demagnetization control at time t_{0+}.

Stator flux space vectors at the fault moment, without and with demagnetization control, are shown in Fig. 7. It is observed that the stator flux amplitude does not change at time t_{0+} in both cases to guarantee the continuity of stator flux and energy. Natural stator current is then enlarged with demagnetizing rotor current, coinciding with the mathematical analysis.

System currents corresponding to the natural component, without and with demagnetization control, are shown in Fig. 8. As discussed before, the energy given by (14) is consumed by the stator resistance during the transient process, indicating that natural stator flux damping is related to the natural stator current. The higher the natural stator current, the more power is consumed by the stator resistance, leading to accelerated natural flux damping. Since natural stator current is enlarged with the demagnetization control, natural stator flux damping is promoted, in accordance with the previous analysis.

IV. LVRT Capability

Two cases are taken as examples to show how the demagnetization control influences the LVRT capability. Grid voltage drops to 70% p.u. in both cases and the grid fault lasted for 70 ms in case 1, while it lasts for 60 ms in case 2. Stator flux trajectories of the DFIG without and with demagnetization control, referred to as system *NDe* and system *De*, respectively, are shown in Fig. 9. Demagnetization control of system *De* is activated during grid fault and immediately disabled on detecting the fault recovery.

DC stator flux of the two systems at grid fault recovery time is shown by the solid black line in the figure. With the same grid fault, $\vec{\psi}_{sn\_De}(t_{0+})$ equals $\vec{\psi}_{sn\_NDe}(t_{0+})$. Since they partially overlap with $\vec{\psi}_{sn\_De}(t_{1+})$ and $\vec{\psi}_{sn\_NDe}(t_{1+})$ in case 2, they are not shown in Fig. 9. However, they can be represented by $\vec{\psi}_{sn}(t_{0+})$ shown in Fig. 5, which is of the same amplitude and space position.

For case 1, it is illustrated in Fig. 9(a) and (b) that we have $\left|\vec{\psi}_{sn}(t_{0+})\right| < \left|\vec{\psi}_{sn}(t_{1+})\right|$ for both systems. In respect that real-time natural EMF is proportional to the dc stator flux, as indicated in (21), we have $|\vec{e}^{\,r}_{rn}(t_{0+})| < |\vec{e}^{\,r}_{rn}(t_{1+})|$, generating a worse condition at time t_{1+} than that at time t_{0+}. Moreover, since dc stator flux damps faster with demagnetization control, it is observed that $\left|\vec{\psi}_{sn\_De}(t_{1+})\right|$ is smaller than $\left|\vec{\psi}_{sn\_NDe}(t_{1+})\right|$ in this case, denoting that demagnetization control makes system *De* have more chance to survive compared with system *NDe*.

Things take different turns in case 2. It is shown in Fig. 9(c) and (d) that now we have $\left|\vec{\psi}_{sn\_NDe}(t_{1+})\right| < \left|\vec{\psi}_{sn\_De}(t_{1+})\right|$. That means comparing with system *NDe*, system *De* goes through a worse condition at time t_{1+}. However, it is noticed that $\left|\vec{\psi}_{sn\_De}(t_{1+})\right|$ is smaller than $\left|\vec{\psi}_{sn}(t_{0+})\right|$ in this case. That is to say, the RSC still has a good chance to survive the fault recovery with demagnetization control in this case.

Fig. 10 shows $\left|\vec{\psi}_{sn\_\mathrm{p.u.}}(t_{1+})\right|$ of the two systems with respect to grid fault duration Δt. As indicated by the analysis, demagnetization control gives the system more chance to survive grid fault recovery when Δt locates in the shadowed area.

To investigate the improvement of LVRT capability for practical wind power system under balanced grid fault, the feasibility region is then defined as the voltage dips where the RSC can successfully survive the grid fault and the fault recovery. However, system ride-through performance is affected by many factors, for instance, system prefault speed, active and reactive current reference, RSC voltage rating, and overcurrent capability. To define the boundary of the feasibility region, a criterion is made that the EMF is constrained to 0.5 p.u. Since $\vec{e}^{\,r}_{rn}$ and $\vec{e}^{\,r}_{rf}$ are at different frequencies, the maximum EMF is approximately the algebraic summation of the values, which can be obtained according to (20) and (22)

$$E^r_{r\max} \approx \begin{cases} (1-P)\,|s|\,V_s + (1-s)\,\dfrac{L_m}{L_s}PV_s (t_0 \le t < t_1) \\ |s|\,V_s + (1-s)\,\dfrac{L_m}{L_s}PV_s \left|e^{-\Delta t/\tau_s} - e^{-j\omega_s \Delta t}\right| \\ \qquad\qquad (t_1 \le t). \end{cases} \tag{28}$$

The feasibility regions for balanced grid fault, with respect to different demagnetization coefficient *K* and prefault system slip s, are shown in Fig. 11 according to (28). The stator flux

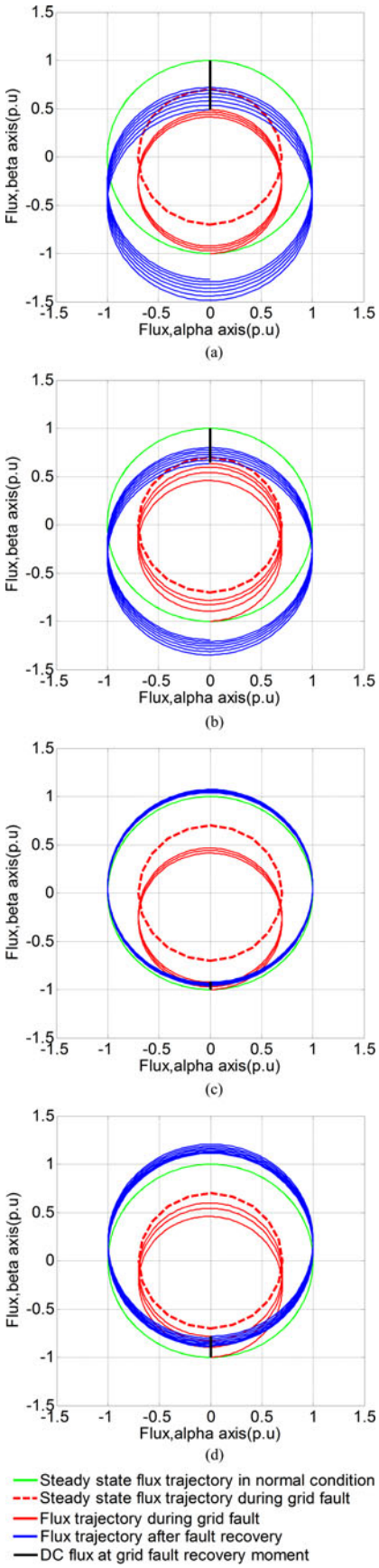

Fig. 9. Stator flux trajectory. (a) System *NDe* in case 1. (b) System *De* in case 1. (c) System *NDe* in case 2. (d) System *De* in case 2.

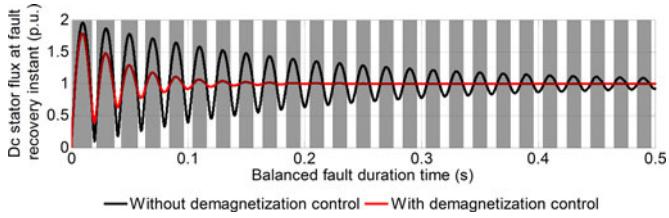

Fig. 10. Normalized dc stator flux at recovery moment for system with and without demagnetization control.

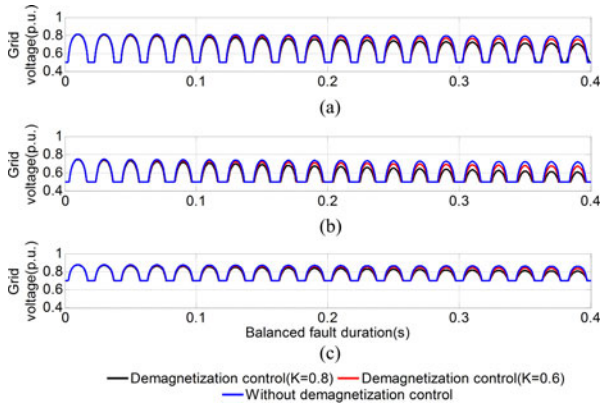

Fig. 11. Feasibility region of the MW level system. (a) $s = 0.2$. (b) $s = 0$. (c) $s = -0.2$.

time constant for the system without demagnetization control is given as $\tau = 1.5\ s$, corresponding to a typical MW-level DFIG. To present the curves clearly, only feasible region for balanced grid fault where the fault duration is less than 0.4 s is shown in the figure. Any point above the curve means that the DFIG can ride through the grid fault and the fault recovery in the corresponding situation.

Several conclusions can be reached from Fig. 11 and (28). First, the maximum acceptable voltage dip depth decreases with higher rotational speed. Second, the improvement induced by demagnetization control is enlarged when the machine works closer to synchronous speed. Third, the higher the demagnetization coefficient, the wider feasibility region can be obtained. To summarize, system LVRT capability is improved with demagnetization control, and greater improvement can be obtained with higher K and smaller $|s|$.

V. Experimental Verification

In order to validate the analysis obtained in the previous sections, several experimental tests were performed using the experimental setup shown in Fig. 12. The configuration of the system is given in Fig. 13.

The following items are included in the test bed:

1) an 11-kW wound rotor machine was used as the DFIG;
2) an 11-kW squirrel cage induction machine (SCIM) was used as the prime mover, which can work at constant speed or constant torque with a motor driver;
3) a 5-kW three-phase programmable ac voltage source was used to generate the balanced voltage sag;

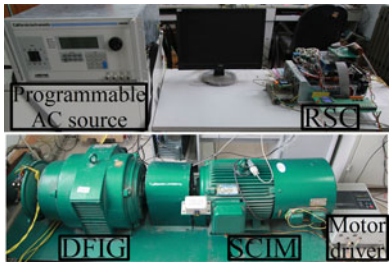

Fig. 12. Experimental setup.

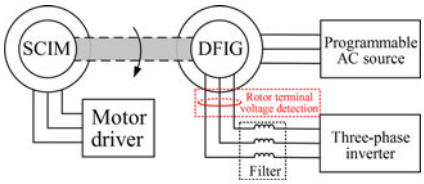

Fig. 13. Configuration of the experimental setup.

4) a three-phase PWM inverter was used as the RSC, the stator and rotor current, stator voltage, and rotor position of the DFIG were detected by sensors;
5) two Oscilloscopes were used to measure the stator and rotor current and stator and rotor terminal voltage. The high-frequency acquisition mode of the oscilloscopes was adopted in the experiment to depress the noise. The rotor terminal voltages were measured at the position shown in Fig. 13, with analog filters with cutoff frequency of 1 KHz in order to remove the switching harmonic of the RSC.

Detailed parameters of the test bed are given in the Appendix. Note that to match the low-power programmable ac power source, the base voltage and current used in the experiment were deliberately reduced, compared with the rated value of the DFIG. A second-order low-pass filter with cutoff frequency of 10 Hz was used to detect dc stator current in demagnetization control in the following experiments.

A. Normal Condition

The system was first tested with no load at the base voltage. Initially, the DFIG was fully excited from the stator side. At time $t = -2.5\,\mathrm{s}$, the speed reference was changed from 900 to 1100 r/min and the reactive current reference was changed from 0 to 3.5 A at $t = 1.5\,\mathrm{s}$. System responses are shown in Fig. 14. Note that the stator current was reduced at $t = 1.5\,\mathrm{s}$, since the magnetizing current was now partly supplied by the rotor.

B. Demagnetization Control

Demagnetization control was then examined with no load. Three systems with different configurations and different control approaches, denoted system *ROC*, system *NDe* and system *De*, respectively, were designed and listed in Table I. The DFIG was operating at 10% above the synchronous speed when the grid voltage dropped to 70% of the rated value at $t_0 = 0\,\mathrm{s}$. Fig. 15 shows the responses of the three systems. The waveform of the

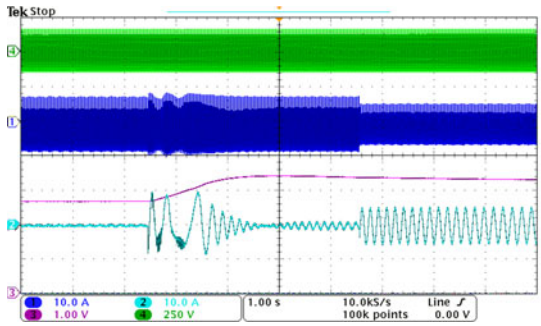

Fig. 14. System performance in normal condition. Ch.1: Stator current (Phase A). Ch.2: Rotor current (Phase A). Ch.3: Rational speed (333RPM per scale). Ch.4: Stator voltage (Phase A).

TABLE I
THREE SYSTEMS IN DEMAGNETIZATION CONTROL EXPERIMENT

	System *ROC*	System *NDe*	System *De*
Rotor condition	Open-circuit	RSC connected	RSC connected
Control strategy	None	FFTCC	FFTCC with demagnetization control ($K = 0.8$)
Rotational speed	Controlled by prime mover	Controlled by DFIG	Controlled by DFIG

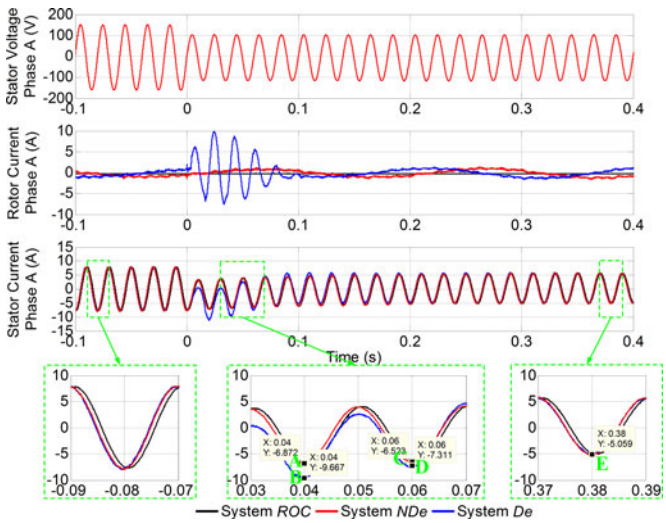

Fig. 15. Response to 30% voltage dip.

stator current of system *ROC* has been deliberately displaced for 1 ms so that it can be perceived.

First, it is noticed that the stator current of system *ROC* and system *NDe* have the same waveforms, which proves the RSC of system *ROC* behaves like an open circuit to the stator natural current under shallow grid fault, as described in Section II. Second, it is obvious that the dc stator current of system *De* damps faster than that of system *NDe*, denoting accelerated dc stator flux damping, as proved mathematically before. Third, it is observed that the envelope of the stator current of system *NDe* is "continuous." In contrast, with the injection of rotor

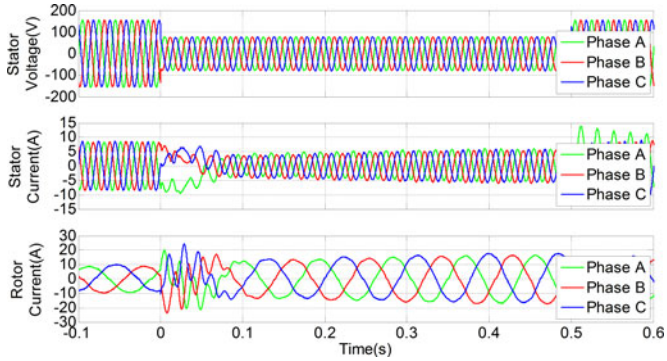

Fig. 16. Performance of system *De*.

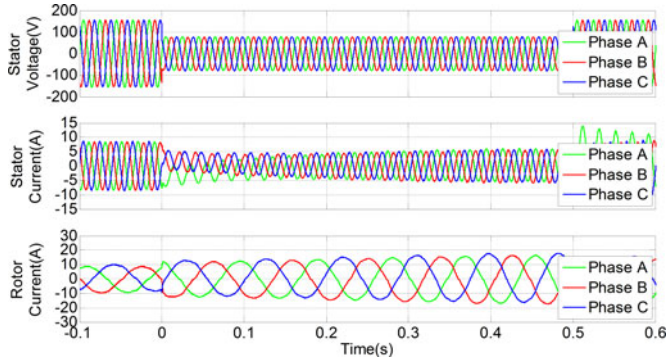

Fig. 17. Performance of system *NDe*.

demagnetizing current, the envelope of stator current of system *De* is enlarged, making it behave like "discontinuous," as explained in Fig. 7(b).

To prove the mathematical derivation, five points, located at negative peak of stator current of system *De* and system *NDe*, are shown in Fig. 15. Take point E as the steady state during grid fault, the dc offset of points A, B, C, D can be obtained as $\mathrm{DC_A} = 1.813$, $\mathrm{DC_B} = 4.608$, $\mathrm{DC_C} = 1.464$, $\mathrm{DC_D} = 2.252$. The stator time constant of the two systems can be derived with the equations of $1 - e^{-0.02/\tau_{NDe}} = (\mathrm{DC_A} - \mathrm{DC_C})/\mathrm{DC_A}$ and $1 - e^{-0.02/\tau_{De}} = (\mathrm{DC_B} - \mathrm{DC_D})/\mathrm{DC_B}$ and given as $\tau_{NDe} = 0.089\,\mathrm{s}$ and $\tau_{De} = 0.027\,\mathrm{s}$. The ratio is given as

$$\tau_{De}/\tau_{NDe} = 0.3. \tag{29}$$

Theoretical ratio can be obtained with (16) and (25) and shown as

$$\tau_{De\_\mathrm{theoretical}}/\tau_{NDe\_\mathrm{theoretical}} = (L_s - KL_m)/L_s = 0.262. \tag{30}$$

Comparing (29) and (30), it is noticed that close agreement is achieved, proving the mathematical derivation in the aforementioned analysis.

C. Active and Reactive Power Control During Grid Fault

To validate the system coordinate control strategy, the system was then tested when it was half loaded, i.e., the input mechanical power was 900 W. The stator voltage dropped to 0.5 p.u. during the grid fault and lasted for 100 ms. The maximum allowed rotor current was set to 1.5 p.u. during grid fault. Performances of system *De* and system *NDe* are given in Figs. 16 and 17, respectively. Demagnetizing rotor current was injected to promote dc stator flux damping in system *De*, which lasted for about 0.1 s. It is noticed that the total current is well limited for both systems. With the coordinate control strategy, it is possible to supply active and reactive power when demagnetization control is activated. Rotational speed and the current components of the two systems are given in Fig. 18.

The reactive current required by the grid was injected right after the grid fault was detected for both systems. It is also observed that active current of system *De* is limited at the beginning of the grid fault due to the injection of demagnetizing current. Since the restriction only lasts for about 0.05 s, it does not make too much trouble for the active power balance of the system, which can be noticed by system rotational speed. Moreover, the pitch control can be activated to reduce the input active power in real application if necessary.

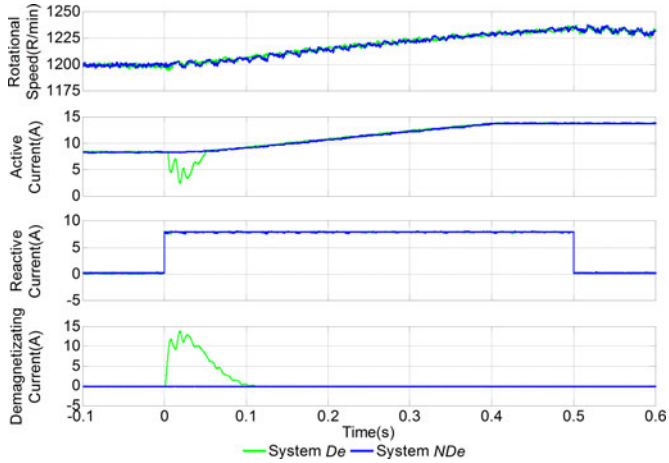

Fig. 18. Rotational speed and current components of system *De* and system *NDe*.

TABLE II
GRID FAULTS

	Fault A	Fault B	Fault C	Fault D
Fault depth	30%	30%	50%	50%
Fault Duration	70 ms	60 ms	70 ms	60 ms

D. LVRT Capability

To demonstrate the influence of demagnetization control on the LVRT capability, four balanced grid faults listed in Table II were designed and tested for system *NDe* and system *De*. To clearly present system response, the experiments were done with no load. The reactive current was not injected during the grid fault for the same reason. Depth of fault A and fault B are small enough that both systems survived the fault and the recovery. Experimental stator flux trajectories are shown in Fig. 19, while the theoretical stator flux trajectories can be found in Fig. 9.

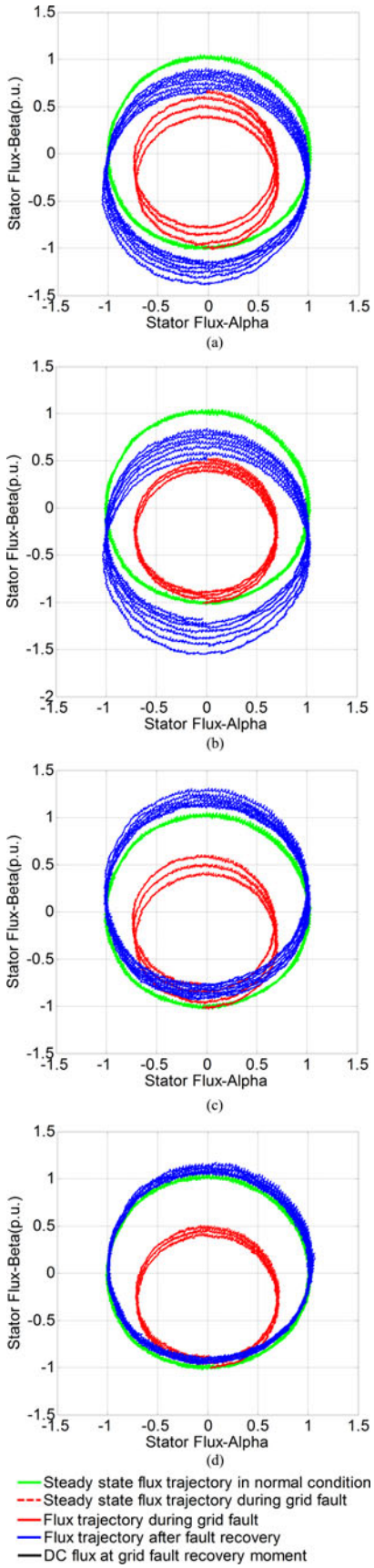

Fig. 19. Experimental stator flux trajectory. (a) System *NDe* in fault A. (b) System *De* in fault A. (c) System *NDe* in fault B. (d) System *De* in fault B.

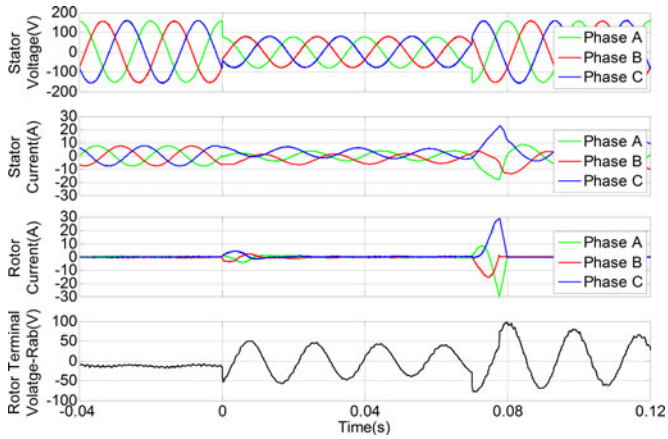

Fig. 20. Reaction of system *NDe* to fault C.

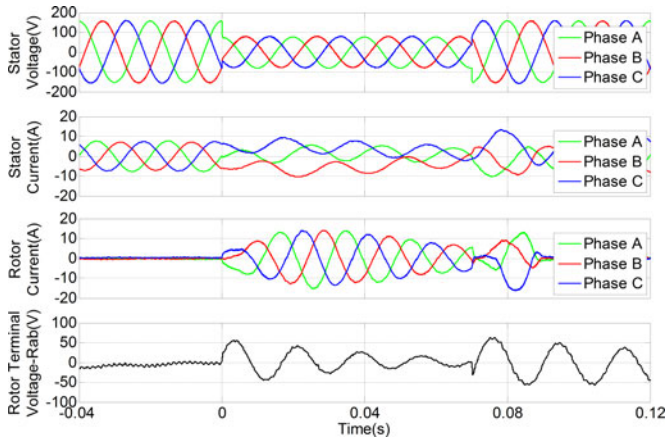

Fig. 21. Reaction of system *De* to fault C.

It is noticed that the experimental results of system *NDe* agree well with the theoretical analysis while that of system *De* differs a little bit from the theoretical results, especially during the first line circle right after the grid fault. The reason is that the low-pass filter adopted in the demagnetization control induces some delay in decomposing the dc stator current, which further delays the injection of the demagnetizing rotor current. After full decomposition of the dc stator current, close agreement is reached between the experimental and the theoretical results.

With severe voltage fault, it is likely that the RSC may survive the grid fault but fail at the fault recovery moment, as what happened with fault C. Performances of system *NDe* and system *De* under grid fault C are shown in Figs. 20 and 21, respectively. Since EMF cannot be measured, it is represented by the rotor terminal voltage, in respect that they differ by a small voltage drop in the rotor circuit impedance.

The systems were operating at 10% above the synchronous speed before the voltage dip. At time $t_0 = 0$ s, the grid fault happened, generating an EMF whose line-to-line peak value reached 50 V. Since it is with in the RSC voltage rating, both systems survived the fault moment. For system *NDe*, the natural stator flux damped very slowly, generating a rotor circuit EMF with a line-to-line peak value of about 100 V at the fault

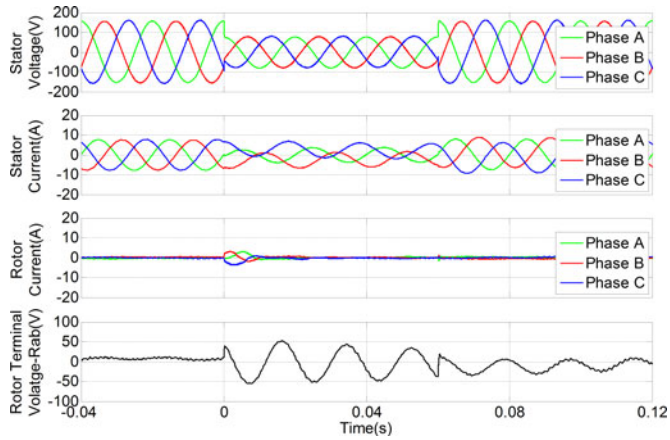

Fig. 22. Reaction of system *NDe* to fault D.

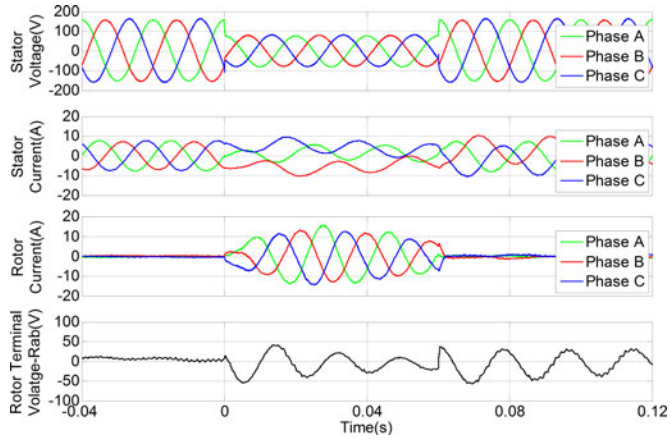

Fig. 23. Reaction of system *De* to fault D.

recovery moment, exceeding the voltage rating of the RSC and trigging the protection element. In contrast, as shown by $\vec{v}^{r}_{rn}$ of system *De*, the natural stator flux damped fast with the rotor demagnetizing current, generating a rotor circuit EMF with a line-to-line peak value of 60 V at the fault recovery moment, which is just a little bit higher than $|\vec{v}^{r}_{rn}\,(t_{0+})|$. Therefore, the system *De* survived fault C, performing better LVRT capability.

Responses of system *NDe* and system *De* to grid fault D are shown in Figs. 22 and 23, respectively. As discussed before, we have $|\vec{e}^{r}_{rn\_De}\,(t_{1+})| > |\vec{e}^{r}_{rn\_NDe}\,(t_{1+})|$ in this case and it is proved by the rotor terminal voltage shown in the two figures. However, because these two values are smaller than $|\vec{e}^{r}_{rn}\,(t_{0+})|$, both systems survived the fault recovery, performing similar LVRT capability.

VI. Conclusion

This paper analyzed the challenges for a DFIG-based wind turbine to ride through a balanced fault. It has shown that the dc stator flux is produced at the fault and recovery moment, resulting in a large EMF in the rotor circuit. An improved demagnetization control, without the information of system parameter, is proposed for the RSC. With the injection of rotor demagnetizing current, the dynamic process is shortened. System LVRT capability with the proposed control is analyzed with the consideration of grid fault duration. It is illustrated that the proposed control minimizes the occurrence of the protection system, especially when the system is running close to synchronous speed. Feasibility region for a representative sized system is also investigated according to the analysis. A test rig has been set up and the experiment results validated the proposed control method and the analysis. The study clearly shows the ability for a DFIG-based wind turbine to ride through the balanced grid fault and the limitations to that control objective. Although it has been proven that the most severe voltage dip cannot be handled by only control techniques [27], the proposed control can be adopted to modify the conventional DFIG-based wind power system.

Appendix

Ratings: $P_n = 11\,\text{kW}$, $U_n = 380\,\text{V}$(line to line, RMS).
Turns ratio: $N_s/N_r = 5/2$.
Pole pairs: 3.
Stator resistance: $R_s = 0.03\,\text{p.u.}$
Stator leakage inductance: $L_{ls} = 0.1677\,\text{p.u.}$
Rotor resistance: $R_r = 0.06\,\text{p.u.}$
Rotor leakage inductance: $L_{lr} = 0.0864\,\text{p.u.}$
Mutual inductance: $L_m = 2\,\text{p.u.}$
DC-link voltage: $V_{\text{DC}} = 32\,\text{V}$.
Rotor circuit filter inductance: $L_f = 0.0582\,\text{p.u.}$
Base stator voltage (line to line, RMS): $V_{s\_\text{base}} = 190\ \text{V}$.
Base stator current (RMS value): $I_{s\_\text{base}} = 5\,\text{A}$.
Base rotor current (RMS value): $I_{r\_\text{base}} = 12.5\,\text{A}$.
Rotor circuit overcurrent threshold (peak value): $I_{r\_\text{overcurrent}} = 29.7\,\text{A}$.

References

[1] F. Blaabjerg and Z. Chen, *Power Electronics for Modern Wind Turbines*. San Rafael, CA, USA: Morgan & Claypool, 2006.
[2] *Grid Code, High and Extra High Voltage*, E.ON Netz GmbH, Bayreuth, Germany, Apr. 2006. [Online]. Available: http://www.eon-netz.com
[3] J. Lopez, P. Sanchis, X. Roboam, and L. Marroyo, "Dynamic behavior of the doubly-fed induction generator during three-phase voltage dips," *IEEE Trans. Energy Convers.*, vol. 22, no. 3, pp. 709–717, Sep. 2007.
[4] J. Lopez, E. Gubia, P. Sanchis, X. Roboam, and L. Marroyo, "Wind turbines based on doubly fed induction generator under asymmetrical voltage dips," *IEEE Trans Energy Convers.*, vol. 23, no. 1, pp. 321–330, Mar. 2008.
[5] G. Pannell, D. J. Atkinson, and B. Zahawi, "Minimum-threshold crowbar for a fault-ride-through grid-code-compliant DFIG wind turbine," *IEEE Trans. Energy Convers.*, vol. 25, no. 2, pp. 750–759, Sep. 2010.
[6] Q. Wei, G. K. Venayagamorthy, and R. G. Harley, "Real-time implementation of a STATCOM on a wind farm equipped with doubly fed induction generators," *IEEE Trans. Ind. Appl.*, vol. 45, no. 1, pp. 98–107, Jan. 2009.
[7] P. S. Flannery and G. Venkataramanan, "A fault tolerant doubly fed induction generator wind turbine using a parallel grid side rectifier and series grid side converter," *IEEE Trans. Power Electron.*, vol. 23, no. 3, pp. 1126–1135, May 2008.
[8] P. S. Flannery and G. Venkataramanan, "Unbalanced voltage sag ride-through of a doubly fed induction generator wind turbine with series grid-side converter," *IEEE Trans. Ind. Appl.*, vol. 45, no. 5, pp. 1879–1887, Sep. 2009.
[9] O. Abdel-Baqi and A. Nasiri, "A dynamic LVRT solution for doubly fed induction generators," *IEEE Trans. Power Electron.*, vol. 25, no. 1, pp. 193–196, Jan. 2010.
[10] C. Wessels, F. Gebhardt, and F. W. Fuchs, "Fault ride-through of a DFIG wind turbine using a dynamic voltage restorer during symmetrical and

asymmetrical grid faults," *IEEE Trans. Power Electron.*, vol. 26, no. 3, pp. 807–815, Mar. 2011.
[11] W. Guo, L. Xiao, and S. Dai, "Enhancing low-voltage ride-through capability and smoothing output power of DFIG with a superconducting fault-current limiter–magnetic energy storage system," *IEEE Trans. Energy Convers.*, vol. 27, no. 2, pp. 277–295, Jun. 2012.
[12] X. Yan, G. Venkataramanan, P. S. Flannery, Y. Wang, Q. Dong, and B. Zhang, "Voltage-sag tolerance of DFIG wind turbine with a series grid side passive-impedance network," *IEEE Trans. Energy Convers.*, vol. 25, no. 4, pp. 1048–1056, Dec. 2010.
[13] J. Yang, J. E. Fletcher, and J. O'Reilly, "A series-dynamic-resistor-based converter protection scheme for doubly-fed induction generator during various fault conditions," *IEEE Trans. Energy Convers.*, vol. 25, no. 2, pp. 422–432, Jun. 2010.
[14] L. Zhou, J. Liu, Y. Zhu, and S. Zhou, "A series reactor based converter protection scheme of doubly fed induction generator for low voltage ride through," in *Proc. IEEE Energy Convers. Congr. Expo.*, Raleigh, NC, USA, Sep. 2012, pp. 2404–2409.
[15] J. Liang, W. Qiao, and R. G. Harley, "Feed-forward transient current control for low-voltage ride-through enhancement of DFIG wind turbines," *IEEE Trans. Energy Convers.*, vol. 25, no. 3, pp. 836–843, Sep. 2010.
[16] J. Liang, F. H. Howard, J. A. Restrepo, and R. G. Harley, "Feed-forward transient compensation control for DFIG wind turbines during both balanced and unbalanced grid disturbances," *IEEE Trans. Ind. Appl.*, vol. 49, no. 3, pp. 1452–1463, May 2013.
[17] F. K. A. Lima, A. Luna, P. Rodriguez, E. H. Watanabe, and F. Blaabjerg, "Rotor voltage dynamics in the doubly fed induction generator during grid faults," *IEEE Trans. Power Electron.*, vol. 25, no. 1, pp. 118–130, Jan. 2010.
[18] S. Xiao, G. Yang, H. Zhou, and G. Hua, "An LVRT control strategy based on flux linkage tracking for DFIG-based WECS," *IEEE Trans. Ind. Electron.*, vol. 60, no. 7, pp. 2820–2832, Jul. 2013.
[19] D. Xiang, L. Ran, P. J. Tavner, and S. Yang, "Control of a doubly fed induction generator in a wind turbine during grid fault ride-through," *IEEE Trans. Energy Convers.*, vol. 21, no. 3, pp. 652–662, Sep. 2006.
[20] J. Lopez, P. Sanchis, E. Gubia, A. Ursua, L. Marroyo, and X. Roboam, "Control of doubly fed induction generator under symmetrical voltage dips," in *Proc. Int. Symp. Ind. Electron.*, Cambridge, U.K., Jul. 2008, pp. 2456–2462.
[21] J. Lopez, E. Gubi, E. Olea, R. Josu, and M. Luis, "Ride through of wind turbines with doubly fed induction generator under symmetrical voltage dips," *IEEE Trans. Ind. Electron.*, vol. 56, no. 10, pp. 4246–4254, Oct. 2009.
[22] S. Hu, X. Lin, Y. Kang, and X. Zou, "An improved low-voltage ride-through control strategy of doubly fed induction generator during grid faults," *IEEE Trans. Power Electron.*, vol. 26, no. 12, pp. 3653–3665, Dec. 2011.
[23] L. Zhou, J. Liu, Y. Zhu, and S. Zhou, "Robust demagnetization control of doubly fed induction generator during grid faults," in *Proc. IEEE 7th Int. Power Electron. Motion Control Conf.*, Harbin, China, Jun. 2012, pp. 1446–1451.
[24] L. Zhou, J. Liu, and S. Zhou, "Research on LVRT capability of DFIG with demagnetization control," in *Proc. IEEE 5th Energy Convers. Congr. Expo.*, Denver, CO, USA, Sep. 2013, pp. 2277–2282.
[25] J. Morren and S. W. H. de Haan, "Short-circuit current of wind turbines with doubly fed induction generator," *IEEE Trans. Energy Convers.*, vol. 22, no. 1, pp. 174–180, Mar. 2007.
[26] L. Yang, Z. Xu, J. Ostergaard, Z. Dong, and K. Wong, "Advanced control strategy of DFIG wind turbines for power system fault ride through," *IEEE Trans. Power Syst.*, vol. 27, no. 2, pp. 713–722, May 2012.
[27] G. Abad, J. Lopez, M. A. Rodriguez, L. Marroyo, and G. Iwanski, *Doubly Fed Induction Machine: Modeling and Control for Wind Energy Generation Applications*. New York, NY, USA: Wiley, 2011.

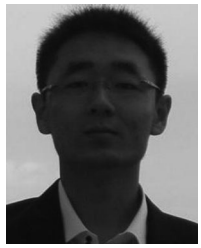

Linyuan Zhou (S'10) received the B.S. degrees in electrical engineering from Xi'an Jiaotong University, Xi'an, China, in 2008, where he is currently working toward the Ph.D. degree at the School of Electrical Engineering.

His current research interests include wind energy, mainly focusing on the low-voltage ride-through performance and output power smoothing.

Jinjun Liu (M'97–SM'10) received the B.S. and Ph.D. degrees in electrical engineering from Xi'an Jiaotong University (XJTU), Xi'an, China, in 1992 and 1997, respectively.

He then joined the teaching faculty of the Electrical Engineering School, XJTU. In 1998, he led the founding of the XJTU/Rockwell Automation Laboratory and served as the Laboratory Director. From 1999 until early 2002, he served as a Visiting Scholar at the Center for Power Electronics Systems, Virginia Polytechnic Institute and State University, USA. He then came back to XJTU and in late 2002 was promoted to a Full Professor and became the Head of the Power Electronics and Renewable Energy Center, XJTU. From 2005 to early 2010, he served as the Associate Dean of the School of Electrical Engineering, XJTU. He is currently the Dean of Undergraduate Education at XJTU. He has coauthored three books, published more than 100 technical papers, holds 24 patents. His research interests include power quality control, renewable energy generation and utility applications of power electronics, and modeling and control of power electronic systems.

Dr. Liu is an AdCom Member of the IEEE Power Electronics Society and serves as the China Liaison. He is also an Associate Editor for the IEEE TRANSACTIONS ON POWER ELECTRONICS. He is an AdCom Member and the Chair of the Student Activities Committee for the IEEE Xi'an Section. He is on the Board of China Electrotechnical Society (CES) and serving as a Vice President for CES Power Electronics Society. He is also the Vice President on International Affairs for the China Power Supply Society. He received several national, provincial, and ministerial awards for scientific and career achievements, including the 2006 Delta Scholar Award.

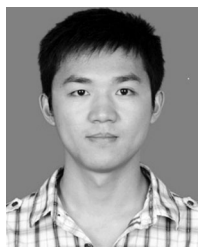

Sizhan Zhou (S'12) received the B.S. degree in electrical engineering from Xi'an Jiaotong University, Shaanxi, China, in 2010, where he is currently working toward the Ph.D. degree at the School of Electrical Engineering, Xi'an Jiaotong University, Xi'an, China.

His current research interests include power quality and renewable energy.